

## Computational Methods for Electromechanical Fields in Self-Assembled Quantum Dots

D. Baretin, S. Madsen, B. Lassen\* and M. Willatzen

*Alision 2, Mads Clausen Institute, University of Southern Denmark,  
DK-6400 Sønderborg, Denmark.*

Received 11 November 2010; Accepted (in revised version) 11 April 2011

Communicated by Xingao Gong

Available online 28 October 2011

---

**Abstract.** A detailed comparison of continuum and valence force field strain calculations in quantum-dot structures is presented with particular emphasis to boundary conditions, their implementation in the finite-element method, and associated implications for electronic states. The first part of this work provides the equation framework for the elastic continuum model including piezoelectric effects in crystal structures as well as detailing the Keating model equations used in the atomistic valence force field calculations. Given the variety of possible structure shapes, a choice of pyramidal, spherical and cubic-dot shapes is made having in mind their pronounced shape differences and practical relevance. In this part boundary conditions are also considered; in particular the relevance of imposing different types of boundary conditions is highlighted and discussed. In the final part, quantum dots with inhomogeneous indium concentration profiles are studied in order to highlight the importance of taking into account the exact In concentration profile for real quantum dots. The influence of strain, electric-field distributions, and material inhomogeneity of spherical quantum dots on electronic wavefunctions is briefly discussed.

**AMS subject classifications:** 82-08

**PACS:** 62.20.-x, 68.65.Hb, 77.65.Ly

**Key words:** Quantum dots, electromechanical fields, continuum model, valence force field, boundary conditions.

---

## 1 Introduction

The understanding of electromechanical fields in nanostructures and their coupling is a topic of ever-increasing interest. Semiconductor nanocrystals serve as an ideal platform for investigating quantum-physics interactions between conduction and valence

---

\*Corresponding author. *Email addresses:* danielle@mci.sdu.dk (D. Baretin), sma@mci.sdu.dk (S. Madsen), benny@mci.sdu.dk (B. Lassen), willatzen@mci.sdu.dk (M. Willatzen)

electrons, phonons, and photons [1,2]. The possibility to control nanostructure geometry (size and shape), material parameters, charge transport, impurities, external fields etc. allows tailoring of device properties towards specific applications [2–11]. Optimization of the latter process (tailoring towards specific device applications) requires determination of coupled strain and electric-field distributions including, in some cases, piezoelectric and electrostrictive effects [12–21]. Eventually, having obtained electromechanical field distributions, properties related to, e.g., quantum computing and optoelectronic devices can be evaluated.

Two routes are traditionally followed in addressing electromechanical field effects based on either atomistic [22–26] or continuum methods [27, 29–31]. While the former are computationally more demanding they provide details on inter-atomic (i.e., lattice constant) scales automatically accounting for the full crystal lattice structure as well as the (location of) specific atoms associated with a lattice point. Evidently, it is expected that these details become increasingly important as nanostructure dimensions approach lattice-constant values. Continuum models, however, are known to provide computationally fast and accurate results for nanostructures with dimensions much larger than a lattice constant. The benefit in using continuum models in terms of reduced computation times makes them preferable (and often unavoidable) for many device calculations where, typically, multiphysics effects such as electromechanical field interactions become important.

To computationally bridge the two regimes of small- or large nanostructures [32], it is necessary to know if atomistic and continuum models can be practically combined for certain applications and to assess qualitatively and quantitatively the level of inaccuracy obtained in using continuum models to evaluate physical properties of smaller nanostructures. Furthermore, an important point which, unfortunately, is largely neglected in the literature, is the discussion of appropriate boundary conditions when computing electromechanical fields.

The goal of the present work is to compare electromechanical field distributions of quantum-dot nanostructures used in novel optoelectronic applications obtained from a continuum electromechanical model and a VFF atomistic method while emphasizing the importance of the chosen boundary conditions.

In the continuum-model case, a total free energy density change  $d\mathcal{U}$  of a piezoelectric medium reads

$$d\mathcal{U} = d\mathcal{U}^{mech} + d\mathcal{U}^{elec} = TdS + \sigma_{ik}d\varepsilon_{ik} + E_idD_i, \quad (1.1)$$

where the mechanical and electrical energy contributions are

$$d\mathcal{U}^{mech} = TdS + \sigma_{ik}d\varepsilon_{ik}, \quad (1.2a)$$

$$d\mathcal{U}^{elec} = E_idD_i, \quad (1.2b)$$

respectively. Here,  $T$ ,  $S$ ,  $\sigma_{ik}$ ,  $\varepsilon_{ik}$ ,  $E_i$ , and  $D_i$  denote the temperature, entropy, stress tensor, strain tensor, electric field, and electric displacement, respectively. For a zincblende

structure assuming isentropic conditions ( $dS=0$ ), the mechanical energy density change becomes using crystal symmetry considerations

$$\begin{aligned} \mathcal{U}^{mech} = & \frac{1}{2}C_{xxxx}(\varepsilon_{xx}^2 + \varepsilon_{yy}^2 + \varepsilon_{zz}^2) + C_{xxyy}(\varepsilon_{xx}\varepsilon_{yy} + \varepsilon_{xx}\varepsilon_{zz} + \varepsilon_{yy}\varepsilon_{zz}) \\ & + 2C_{xyxy}(\varepsilon_{xy}^2 + \varepsilon_{xz}^2 + \varepsilon_{yz}^2) + \mathcal{U}_{ref}^{mech}, \end{aligned} \quad (1.3)$$

where  $C_{ijkl}$  are constant parameters and  $\mathcal{U}_{ref}^{mech}$  is the reference mechanical energy corresponding to an unstrained structure.

We derive in the framework of the continuum model and the above expression for the total energy governing electromechanical equations based on Newton's Second Law for a solid elastic nanocrystal, the Maxwell-Poisson equation, and piezoelectric constitutive equations.

The VFF-based models rely on a phenomenologically expression of the free energy  $F$  [1]:

$$\begin{aligned} F = & \frac{1}{2} \left[ \sum_{ij} c_1 (\delta \mathbf{r}_{ij})^2 + \sum_{ik} c_2 (\delta \mathbf{r}_{ik})^2 + \sum_{BAB} c_3 \mathbf{r}_0^2 (\delta \theta_{ijk})^2 + \sum_{ABA} c_4 \mathbf{r}_0^2 (\delta \theta_{jkl})^2 \right. \\ & \left. + \sum_{BAB} c_5 \mathbf{r}_0 (\delta \theta_{ijk}) (\delta |\mathbf{r}|_{ij}) + \sum_{ABA} c_7 \mathbf{r}_0 (\delta \theta_{jkl}) (\delta |\mathbf{r}|_{jk}) + \dots \right], \end{aligned} \quad (1.4)$$

assuming two atoms  $A$  and  $B$  per unit cell. The first two terms in Eq. (1.4) correspond to bond stretching forces,  $j$  and  $k$  denote, respectively, the nearest- and next-nearest neighbors of an atom  $i$ . The remaining terms represent bond bending forces. Quantities  $\delta \mathbf{r}_{ik}$  and  $\delta \theta_{ijk}$  represent changes in position vectors and angles from their reference values, respectively.

In this work, the atomistic free energy of the InAs/GaAs quantum-dot structure is constructed introducing position-dependent  $\alpha$  and  $\beta$  coefficients and atomic-position values. Interpolation schemes so as to handle heterostructures are presented and explained. Furthermore, the implementation of the VFF free-energy minimization method corresponding to an equilibrium heterostructure configuration is discussed and two methods for the calculation of strain fields based on results of VFF calculations are compared. And finally, a method for the incorporation of the piezoelectric effect is given.

For numerical calculations it is necessary to significantly reduce the size of the domain in which computations are performed relative to the size of the structure in reality. A section is dedicated to the problem of choosing boundary conditions on the computational domain so as to correctly capture the strain fields in the vicinity of the quantum dot while keeping computational cost to a minimum, i.e., keeping memory requirements and computational time as low as possible.

In the final two sections results are presented for quantum dots with spherical, cubic, and truncated pyramidal shapes. Investigation of quantum-dot size and shape effects based on the continuum and VFF atomistic methods are performed. The discussion is continued to encompass strain values and differences between the two models

for off-diagonal strain values are highlighted [33,34]. Further, results on the influence of concentration gradients are presented. An important structure for use in optoelectronic applications is the quantum-dot wetting-layer structure [35–37,41,42]. The computation of periodic quantum-dot structures is briefly addressed. The final part of this section involves a comparison between electromechanical fields obtained by interpolation of In and Ga material parameters (effective-medium approximation) at lattice sites. Finally, a discussion is presented for strain and electric field results in two cases corresponding to (i) a homogeneous concentration inside a spherical quantum dot, and (ii) a linear concentration profile from the center of the spherical dot to its radius.

## 2 Structures under consideration

We consider three different InAs/GaAs quantum dot shapes, a spherical, a cubic, and a truncated pyramidal shape as shown in Figs. 1 and 2. The truncated pyramidal quantum dot structure has been chosen as this more closely resembles InAs/GaAs quantum dots formed by the Stranski-Krastanov growth process [43,44]. Most of the comparisons are, however, performed using the spherically-shaped quantum dot. We do this in order to focus on size and concentration profile effects rather than macroscopic shape effects.

The corresponding atomistic structure of the spherical, the cubic, and the truncated pyramidal quantum dot used in this work is shown in Figs. 3 and 4.

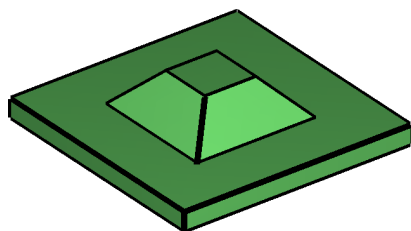


Figure 1: Continuum view of the truncated pyramidal quantum dot with wetting layer.

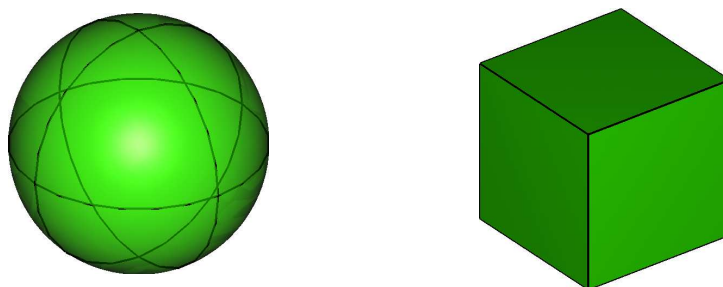


Figure 2: Continuum view of the spherical and cubic quantum dots considered in this work.

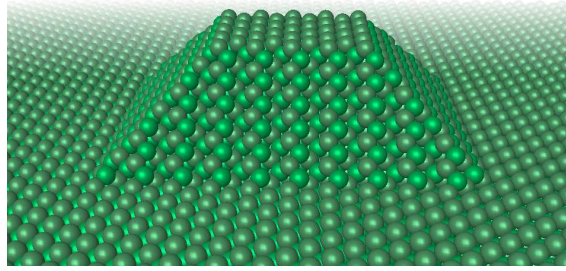


Figure 3: Atomistic view of the truncated pyramid with wetting layer.

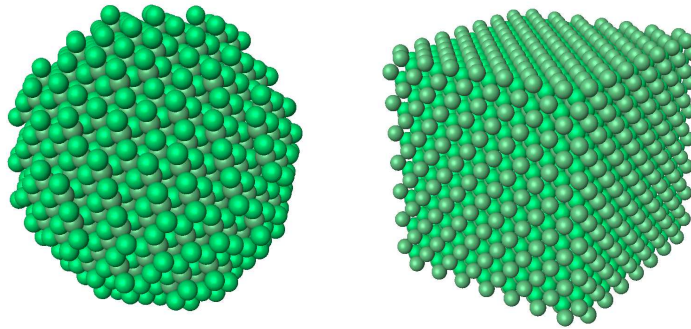


Figure 4: Atomistic view of the spherical and cubic quantum dots considered in this work.

### 3 Governing equations for the continuum model

#### 3.1 Fundamental equations

In this Section, we derive the governing equations in the continuum model framework accounting for mechanical, electrical, and piezoelectric effects. Repeated reference is made to [45].

##### 3.1.1 The strain tensor

Under the action of applied forces, solid bodies exhibit a deformation changing their shape and volume [45]. Assume the position of a point before the deformation is given by the position vector  $\mathbf{r}$  (with components  $x_1 = x$ ,  $x_2 = y$ ,  $x_3 = z$ ). After the deformation, the point, originally at  $\mathbf{r}$ , is now at  $\mathbf{r}'$  (with components  $x'_i$ ). The displacement vector is defined as follows:

$$\mathbf{u} = \mathbf{r}' - \mathbf{r}, \quad (3.1)$$

with components  $u_i = x'_i - x_i$ . The distance between two points of the body is given by  $dl = \sqrt{dx_1^2 + dx_2^2 + dx_3^2}$  and  $dl' = \sqrt{dx_1'^2 + dx_2'^2 + dx_3'^2}$  before and after the deformation, re-

spectively. Using  $dx'_i = dx_i - du_i$  and substituting  $du_i = (\partial u_i / \partial x_k) dx_k$  yield:

$$dl'^2 = dl^2 + 2\varepsilon_{ik} dx_i dx_k, \quad (3.2)$$

where the *strain tensor*,  $\varepsilon_{ik}$  has been introduced:

$$\varepsilon_{ik} = \frac{1}{2} \left( \frac{\partial u_i}{\partial x_k} + \frac{\partial u_k}{\partial x_i} + \frac{\partial u_l}{\partial x_i} \frac{\partial u_l}{\partial x_k} \right). \quad (3.3)$$

In almost all cases when a body is subject to a small deformation all the components of the strain tensor are small (for exceptions see [45]). This allows us to neglect the last term in (3.3) being of second order in smallness

$$\varepsilon_{ik} = \frac{1}{2} \left( \frac{\partial u_i}{\partial x_k} + \frac{\partial u_k}{\partial x_i} \right). \quad (3.4)$$

### 3.1.2 The stress tensor

For a body in mechanical equilibrium the sum of all forces is equal to zero everywhere. In the presence of deformations, internal molecular forces, defined as *internal stresses*, tend to return any body portion to equilibrium. These forces are near-action forces, stemming from the surrounding parts, that act on the surface of the body. In order to express these forces, we have to consider the sum of all forces on all volume elements  $dV$ :  $\int f_i dV$ , where  $f_i$  is the force per unit volume. According to Newton's Third Law, they are equal to the sum of all forces exerted by the surrounding parts which is represented by an integral over the surface of the portion.

From standard vector analysis it is known that an integral of a vector over an arbitrary volume can be transformed into an integral over the surface of the volume if the vector is the divergence of a tensor of rank two (generalized Gauss equation), thus

$$\int f_i dV = \int \frac{\partial \sigma_{ik}}{\partial x_k} dV = \oint \sigma_{ik} dA_k, \quad (3.5)$$

with

$$f_i = \frac{\partial \sigma_{ik}}{\partial x_k}. \quad (3.6)$$

The tensor  $\sigma_{ik}$  is called the stress tensor, and  $\sigma_{ik} dA_k$  is the  $i$ 'th component of the force on the surface elements  $dA_k$ . Disregarding net angular momentum forces leads to a symmetric stress tensor [45]

$$\sigma_{ik} = \sigma_{ki}. \quad (3.7)$$

In mechanical equilibrium the internal stresses in every volume element must be balanced, i.e.,  $f_i = 0$ , or

$$\frac{\partial \sigma_{ik}}{\partial x_k} = 0. \quad (3.8)$$

### 3.1.3 Free energy

An expression for the free energy density as a function of the strain tensor is derived next.

Multiplying the force  $f_i = \partial\sigma_{ik}/\partial x_k$  by the displacement  $\delta u_i$  and integrating over the volume  $V$  the work  $\delta W$  done by the internal stresses per unit volume can be calculated as

$$\int \delta W dV = \int \left( \frac{\partial\sigma_{ik}}{\partial x_k} \right) \delta u_i dV. \quad (3.9)$$

Integrating by parts and assuming an infinite medium to be undeformed at infinity [45]

$$\delta W = \sigma_{ik} \delta \varepsilon_{ik}, \quad (3.10)$$

the expression for the internal mechanical energy  $dU^{mech.}$  at thermodynamic equilibrium for a reversible process at temperature  $T$  becomes:

$$dU^{mech.} = TdS - dW = TdS + \sigma_{ik} d\varepsilon_{ik}, \quad (3.11)$$

where  $S$  is the entropy of the system. Introducing the Helmholtz free energy of the body  $\mathcal{F} = U - TS$ , we obtain

$$d\mathcal{F} = -SdT + \sigma_{ik} d\varepsilon_{ik}. \quad (3.12)$$

Then, assuming isothermal conditions:

$$\sigma_{ik} = \left( \frac{\partial\mathcal{F}}{\partial\varepsilon_{ik}} \right). \quad (3.13)$$

The idea is to expand  $\mathcal{F}$  in powers of  $\varepsilon_{ik}$  assuming small deformations. The general form of the free energy density to second order in  $\varepsilon_{ik}$  for a deformed crystal is given by [45]

$$\mathcal{F} = \frac{1}{2} C_{iklm} \varepsilon_{ik} \varepsilon_{lm}, \quad (3.14)$$

where  $C_{iklm}$  is a rank four *elastic modulus tensor* with the following symmetry properties

$$C_{iklm} = C_{kilm} = C_{ikml} = C_{lmik}. \quad (3.15)$$

Using Eq. (3.13) the stress tensor for a crystal in terms of strain tensor is given by

$$\sigma_{ik} = C_{iklm} \varepsilon_{lm}. \quad (3.16)$$

The elastic modulus tensor is usually expressed also as  $C_{\alpha\beta}$ , with  $\alpha$  and  $\beta$  taking values from 1 to 6 in correspondence with  $xx, yy, zz, yz, zx, xy$  (Voigt notation).

### 3.1.4 Constitutive relations

For a dielectric material there is an additional electric contribution to Eq. (3.11)

$$d\mathcal{U}^{elec.} = E_i dD_i, \quad (3.17)$$

where  $\mathbf{E}$  and  $\mathbf{D}$  are the electric field and electric displacement vectors, respectively. The total internal energy density now reads:

$$d\mathcal{U} = TdS + \sigma_{ik} d\varepsilon_{ik} + E_i dD_i. \quad (3.18)$$

In a similar way, the enthalpy is defined by:

$$d\mathcal{H} = TdS - \varepsilon_{ik} d\sigma_{ik} - D_i dE_i. \quad (3.19)$$

Applying the chain rule to derivatives of  $\mathcal{U}$  and  $\mathcal{H}$  it is possible to obtain thermodynamic identities assuming isentropic conditions:

$$e_{ikl} = \left( \frac{\partial D_i}{\partial \varepsilon_{kl}} \right) = - \left( \frac{\partial \sigma_{kl}}{\partial E_i} \right) \quad (\text{piezoelectric coefficient}), \quad (3.20a)$$

$$\hat{\varepsilon}_{ik} = \left( \frac{\partial D_i}{\partial E_k} \right) \quad (\text{permittivity tensor}), \quad (3.20b)$$

$$C_{iklm} = \left( \frac{\partial \sigma_{ik}}{\partial \varepsilon_{lm}} \right) \quad (\text{elastic modulus tensor}). \quad (3.20c)$$

For a small isentropic variation:

$$dD_i = \left( \frac{\partial D_i}{\partial E_k} \right) dE_k + \left( \frac{\partial D_i}{\partial \varepsilon_{kl}} \right) d\varepsilon_{kl} = \hat{\varepsilon}_{ik} dE_k + e_{ikl} d\varepsilon_{kl}, \quad (3.21a)$$

$$d\sigma_{kl} = \left( \frac{\partial \sigma_{kl}}{\partial E_i} \right) dE_i + \left( \frac{\partial \sigma_{kl}}{\partial \varepsilon_{mn}} \right) d\varepsilon_{mn} = -e_{ikl} dE_i + C_{klmn} d\varepsilon_{mn}, \quad (3.21b)$$

and the constitutive relations become in the linear limit:

$$D_i = \hat{\varepsilon}_{ik} E_k + e_{ikl} \varepsilon_{kl}, \quad (3.22a)$$

$$\sigma_{kl} = -e_{ikl} E_i + C_{klmn} \varepsilon_{mn}. \quad (3.22b)$$

## 3.2 Strain field in a quantum dot

The lattice constants in semiconductor heterostructures vary with coordinates, and the lattice mismatch between the quantum dot structure and the matrix material in which it is embedded generates an intrinsic local strain field different from zero [27]. The free elastic energy can be written as:

$$F = \int_V d\mathbf{r} \frac{1}{2} C_{iklm}(\mathbf{r}) \varepsilon_{ik}(\mathbf{r}) \varepsilon_{lm}(\mathbf{r}), \quad (3.23)$$

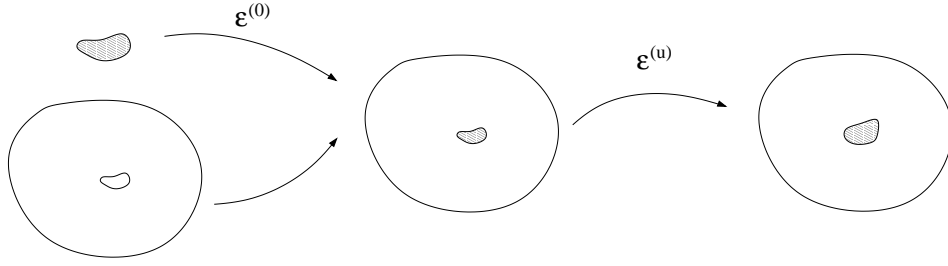


Figure 5: Tensor of local intrinsic strain and local strain tensor.

where  $V$  is the total volume of the system. To take into account lattice mismatch (see Fig. 5), the strain tensor is represented as ( $i, j = x, y, z$ ):

$$\varepsilon_{ij} = \varepsilon_{ij}^{(u)} + \varepsilon_{ij}^{(0)}, \quad (3.24)$$

where  $\varepsilon_{ij}^{(0)}$  is the tensor of local intrinsic strain and  $\varepsilon_{ij}^{(u)}$  is the local strain tensor dependent on positions, given by Eq. (3.4).

### 3.2.1 Zincblende quantum dot

The elastic free energy density for a crystal with zincblende symmetry reads [27]:

$$\mathcal{F} = \frac{1}{2} [C_{11}(\varepsilon_{xx}^2 + \varepsilon_{yy}^2 + \varepsilon_{zz}^2) + 2C_{12}(\varepsilon_{xx}\varepsilon_{yy} + \varepsilon_{xx}\varepsilon_{zz} + \varepsilon_{yy}\varepsilon_{zz}) + 4C_{44}(\varepsilon_{xy}^2 + \varepsilon_{xz}^2 + \varepsilon_{yz}^2)], \quad (3.25)$$

since the only linearly independent elastic constants for a zincblende structure are given by

$$C_{1111} \equiv C_{11}, \quad C_{1122} \equiv C_{12}, \quad C_{2323} \equiv C_{44}. \quad (3.26)$$

The intrinsic strain tensor is given by

$$\varepsilon_{ij}^{(0)} = \delta_{ij}a, \quad (3.27)$$

with

$$a = \frac{a_{matrix} - a_{QD}}{a_{QD}} \quad (3.28)$$

in the dot and zero otherwise [46]. Here  $a_{matrix}$  and  $a_{QD}$  are the lattice constants of the matrix and the quantum dot, respectively. Instead of Eq. (3.28) it is also possible to use the following expression [27]

$$a = \frac{a_{matrix} - a_{QD}}{a_{matrix}}. \quad (3.29)$$

The difference between Eqs. (3.28) and (3.29) is of second order in the strain and, hence, insignificant in linear strain theory.

### 3.3 Piezoelectric field in a quantum dot

Semiconductors can develop an electric polarization with magnitude proportional to the stress subject to an applied stress [27,28]. The induced polarization is related to the strain tensor by the piezoelectric coefficients Eq. (3.20):

$$P_i = e_{ilm}\varepsilon_{lm}, \quad (3.30)$$

where the index  $ilm$  runs over the spatial coordinates.

However, for wurtzite materials we must include an additional contribution due to spontaneous polarization  $P_{sp}$  whose direction depends on the last anion or cation at the surface. The total polarization generates a piezoelectric field  $E_p$  that can be determined, in the absence of external charges, by solving the Maxwell-Poisson equation:

$$\frac{\partial D_i}{\partial x_i} = 0, \quad (3.31)$$

where the displacement vector  $\mathbf{D}$  is given by the first of Eq. (3.22b).

#### 3.3.1 Zincblende quantum dot

There is only one piezoelectric coefficient for a zincblende structure:

$$e_{123} = e_{231} = e_{312} = e_{14}, \quad (3.32)$$

where the latter expression is using Voigt notation. The polarization can be expressed by:

$$P_x = e_{14}\varepsilon_{yz}, \quad P_y = e_{14}\varepsilon_{xz}, \quad P_z = e_{14}\varepsilon_{xy}, \quad (3.33)$$

and the permittivity tensor reads:

$$\epsilon_{ij} = \epsilon\delta_{ij}, \quad (3.34)$$

where  $\epsilon$  is the static dielectric constant of the material.

### 3.4 Governing electromechanical field equations

The governing equations for the electromechanical fields in a heterostructure quantum dot are given by the above-mentioned equilibrium Eq. (3.8)-also known as Navier's static equations-and the Maxwell-Poisson Eq. (3.31):

$$\frac{\partial \sigma_{ij}}{\partial x_j} = 0, \quad \frac{\partial D_i}{\partial x_i} = 0. \quad (3.35)$$

Eq. (3.35) constitute a set of four coupled equations in the electromechanical fields. The expressions for the stress tensor and the electric displacement, given by the constitutive relations (3.22b), can finally be written as:

$$\sigma_{ij} = C_{ijlm}\varepsilon_{lm} + e_{ijm}\frac{\partial V}{\partial x_m}, \quad D_i = -\epsilon_{ij}\frac{\partial V}{\partial x_j} + e_{ilm}\varepsilon_{lm} + P_{sp,i}, \quad (3.36)$$

Table 1: The material parameters [36].  $\epsilon_0$  is the vacuum permittivity.

Quantity		Unit	Value for $\text{In}_c\text{Ga}_{1-c}\text{As}$
Lattice constant	$a$	Å	$5.6503 + 0.4050c$
Elastic constant	$C_{11}$	GPa	$118.8 - 35.5c$
Elastic constant	$C_{12}$	GPa	$53.8 - 8.5c$
Elastic constant	$C_{14}$	GPa	$59.4 - 19.8c$
Piezoelectric constant	$e_{14}$	$\text{Cm}^{-2}$	$0.160 - 0.115c$
Static dielectric constant	$\epsilon$	$\epsilon_0$	$13.18 + 1.42c$

where  $V$  is the electric potential.

In Table 1 we give the material parameters we use for the continuum model [36].

## 4 The valence force field method

The elastic strain energy is subject to different physical constraints, such as invariance under translation and rotation and symmetries due to the crystal structure. Starting from the assumption that the elastic energy depends only on atomic positions, Keating derived an energy invariant under the above symmetries [24]. We will here briefly outline the derivation of the Keating valence force field model. In the following indexes usually refer to an atomic numbering, not spatial coordinates. Since the energy,  $F_{VFF}$ , must be invariant under translation of the crystal as a whole, it must have the functional form  $F_{VFF} = F_{VFF}(\mathbf{r}_{ij})$ , where  $\mathbf{r}_{ij}$  is the difference vector between the atomic positions of atom  $i$  and atom  $j$ . This difference vector is, however, not invariant under a rigid rotation of the crystal, but the scalar product  $\mathbf{r}_{ij} \cdot \mathbf{r}_{kl}$  is. The energy must therefore be a function of such scalar products, leading to the definition of the argument of the elastic energy,  $F_{VFF} = F_{VFF}(\lambda_{ijkl})$ , as

$$\lambda_{ijkl} = \frac{(\mathbf{r}_{ij} \cdot \mathbf{r}_{kl} - \mathbf{R}_{ij} \cdot \mathbf{R}_{kl})}{d_{ij}d_{kl}}, \quad (4.1)$$

where  $\mathbf{R}_{ij}$  is the difference vector between atoms  $i$  and  $j$  in the undeformed crystal and  $d_{ij} = |\mathbf{R}_{ij}|$ <sup>†</sup>. The numerator is chosen so as to make  $\lambda_{ijkl}$  vanish for zero deformation, hence  $\lambda_{ijkl}$  is a suitable basis for a series expansion of the elastic energy. Including up to second-order terms, the energy becomes

$$F_{VFF} = \sum_{i,j,k,l,p,q,r,s} \frac{1}{2} B_{ijkl}^{pqrs} \lambda_{ijkl} \lambda_{pqrs} + \mathcal{O}(\lambda^3). \quad (4.2)$$

The constant term in the expansion is not important and has been left out. The linear terms in  $\lambda_{ijkl}$  must vanish to make the energy an extremum at equilibrium ( $\mathbf{r}_{ij} = \mathbf{R}_{ij}$ ). To ensure also a definite minimum at equilibrium,  $B_{ijkl}^{pqrs}$  must be positive definite.

<sup>†</sup>In [36] defines "d" such that  $4d$  is the lattice constant.

The expansion in Eq. (4.2) includes a huge number of parameters in  $B_{ijkl}^{pqrs}$ , but many of these may be very close to zero or dependent of the other parameters.  $\lambda_{ijkl}$  contains more coordinates than needed to specify the arrangement of  $N$  atoms, in fact only  $3N-6$  coordinates are (usually) needed for this. To reduce the number of parameters, Keating considers only diagonal products of  $\lambda_{ijkl}$  and nearest neighbor interactions. This corresponds to defining  $B_{ijkl}^{pqrs}$  as

$$B_{ijkl}^{pqrs} = \left( \frac{3}{4} \alpha_{ij} d_{ij}^2 \delta_{lj} + \frac{3}{4} \beta_{ijl} d_{ij} d_{il} (1 - \delta_{lj}) \right) \delta_{pi} \delta_{qj} \delta_{rk} \delta_{sl} \delta_{ik}, \quad (4.3)$$

where  $j$  and  $l$  are nearest neighbors to atom  $i$  and the free energy is then obtained as [47]

$$F_{VFF} = \sum_{i,j,l} \left[ \frac{3\alpha_{ij}}{8d_{ij}^2} (\mathbf{r}_{ij} \cdot \mathbf{r}_{ij} - d_{ij}^2)^2 + \frac{3\beta_{ijl}}{8d_{ij}d_{il}} (\mathbf{r}_{ij} \cdot \mathbf{r}_{il} - d_{ij}d_{il} \cos(\Theta_{ijl}))^2 \right], \quad (4.4)$$

where  $\Theta_{ijk}$  is the ideal unrelaxed tetrahedral bond angle and  $\alpha_{ij}$  and  $\beta_{ij}$  are empirical elastic parameters. A two parameter model is obtained if  $d_{ij}$ ,  $\Theta_{ijk}$ ,  $\alpha_{ij}$  and  $\beta_{ijk}$  do not depend on the atomic indexes. In this case,  $d_{ij}^2 \equiv d^2 = 3a^2$ , where  $a$  is the lattice constant.

To obtain the equilibrium atomic positions, the free energy in Eq. (4.4) must be minimized. Popular choices for this minimization are conjugate gradient and the  $L$ -BFGS method [49]. We use the  $L$ -BFGS quasi-Newton method implemented in the SEAM software package [48].

In iteration  $j+1$  of the BFGS method, an approximation to the inverse Hessian,  $\mathbf{H}_{j+1}^{-1}$ , is constructed by

$$\mathbf{H}_{j+1}^{-1} \approx \mathbf{H}_j^{-1} + \frac{\mathbf{s}_j^t \mathbf{y}_j + \mathbf{y}_j^t \mathbf{H}_j^{-1} \mathbf{y}_j}{\mathbf{s}_j^t \mathbf{y}_j} \mathbf{s}_j \mathbf{s}_j^t - \frac{\mathbf{H}_j^{-1} \mathbf{y}_j \mathbf{s}_j^t + \mathbf{s}_j \mathbf{y}_j^t \mathbf{H}_j^{-1}}{\mathbf{s}_j^t \mathbf{y}_j}. \quad (4.5)$$

$\mathbf{H}_j$  is a  $N \times N$  matrix,  $\mathbf{s}_j$  and  $\mathbf{y}_j$  are column vectors,  $\mathbf{s}_j^t$  denotes the transpose (row vector), and  $N$  is the number of elements to optimize (three times the number of atoms in the system). The vectors are

$$\mathbf{s}_j = \frac{\Delta \mathbf{x}_j}{|\Delta \mathbf{x}_j|} \quad \text{and} \quad \mathbf{y}_j = \mathbf{g}_{j+1} - \mathbf{g}_j, \quad (4.6)$$

where  $\mathbf{g}$  is the gradient of the (Keating) energy. Updating of the atomic positions,  $\mathbf{x}_j$ , is done with the scaled Newton step  $\mathbf{x}_{j+1} = \mathbf{x}_j + \Delta \mathbf{x}_{j+1}$  with

$$\Delta \mathbf{x}_{j+1} = -k_{j+1} \mathbf{H}_{j+1}^{-1} \mathbf{g}_{j+1}, \quad (4.7)$$

where  $k_{j+1}$  is a scale factor obtained by minimizing the energy in the  $-\mathbf{H}_{j+1}^{-1} \mathbf{g}_{j+1}$  direction.

In the limited memory BFGS method ( $L$ -BFGS), Eq. (4.5) is used recursively  $m$  times, starting from an initial approximation (e.g., a scaled identity matrix). Since the matrix-vector product in the Newton iteration,  $\mathbf{H}_j^{-1} \mathbf{g}_j$ , can be done efficiently in-place [49], the

method requires only storage of the atomic positions and gradients of the last  $m$  iterations. In our calculations we have used  $m = 5$ , based on the performance of a few test cases.

#### 4.1 Strain tensor from atomistic data

For each atom, a displacement vector can be defined but the classical continuous strain tensor involves derivatives of the displacement vector which are not well-defined in the discrete case. To overcome these difficulties, two methods for calculating strain tensors are compared. One method calculates the displacement vectors for each atom and uses Shepard's interpolation [50] to calculate a continuous displacement vector which can be differentiated in order to calculate the strain tensor. Lattice-mismatch is included by manually subtracting it from the diagonal components when inside the dot. The other method follows [51] where, for atom  $i$ , a discrete deformation gradient,  $\hat{\mathbf{F}}_i$ , is defined by doing a least square minimization on the "error"

$$\phi^i = \sum_j (\mathbf{r}_{ij} - \hat{\mathbf{F}}_i \mathbf{R}_{ij})^2, \quad (4.8)$$

with respect to the components of  $\hat{\mathbf{F}}_i$ .  $j$  runs over the nearest neighbors to atom  $i$ , but may in general run over all atoms by including a weighting factor in the "error" above. The strain is calculated from the discrete deformation gradient as

$$\varepsilon_{lm} = \frac{1}{2} ((\hat{\mathbf{F}}_i^t \hat{\mathbf{F}}_i)_{lm} - \delta_{lm}). \quad (4.9)$$

Lattice mismatch is included automatically if the unstrained bond lengths of the dot material is used inside the dot.

Fig. 6 shows a comparison of the two methods. They are seen to give quite similar results for the strain tensor components. However, in our experience, the interpolation method generally shows more wiggles and spikes than the atomic calculation. Since the atomic method is computationally simpler and faster, this method is a good choice. The wiggles and spikes seen in the method using interpolation depend highly on the choice of trivariate interpolation method.

#### 4.2 Piezoelectric effect based on valence force field calculations

The piezoelectric effect is not taken into account in the VFF model used in this work as only nearest neighbor interactions are included. However, it is possible to include the piezoelectric effect in a so called semi-coupled manner by calculating the electric potential using Gauss's law:

$$\frac{\partial D_i}{\partial x_i} = 0, \quad (4.10)$$

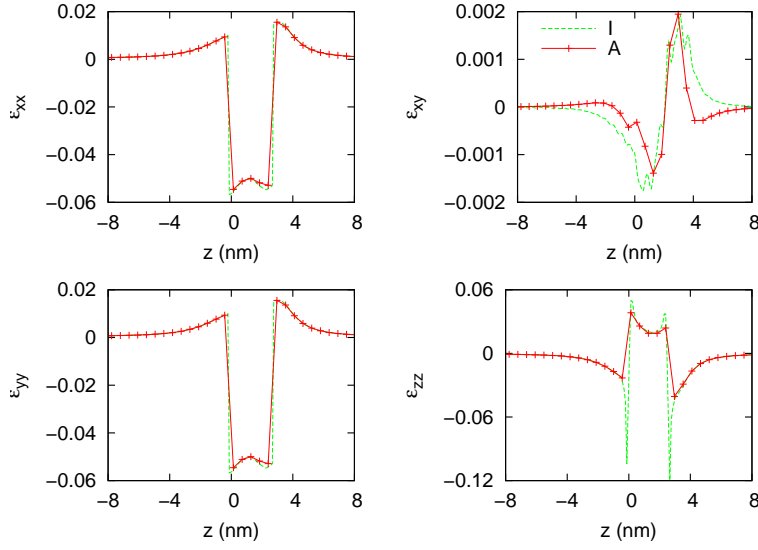


Figure 6: Comparison of the interpolation (I) and atomic (A) methods for calculating the strain tensor on the pyramid structure. The crosses marks the positions of the atoms. The components are evaluated at the center of the dot at different  $z$ -positions.  $\varepsilon_{xz} = \varepsilon_{yz} = 0$  are not shown.

with

$$D_i = -\varepsilon_{ij} \frac{\partial V}{\partial x_j} + e_{ilm} \varepsilon_{lm}, \quad (4.11)$$

where  $\varepsilon_{lm}$  is interpolated strain fields based on VFF calculations. This approach is called semi coupled because the electric field is coupled to the strain fields but the strain fields are independent of the electric field [52]. It has previously been shown that the semi-coupled approach works well for most zinc-blende compounds [53], in particular the InAs/GaAs system considered in this work.

## 5 Connection between continuum and VFF

For bulk materials ( $d_{ij}$ ,  $\alpha_{ij}$  and  $\beta_{ij}$  independent on atomic index),  $\alpha$  and  $\beta$  can be expressed in terms of  $C_{11}$  and  $C_{12}$  as [47]

$$\alpha = \frac{1}{\sqrt{3}}(C_{11} + 3C_{12})d, \quad (5.1a)$$

$$\beta = \frac{1}{\sqrt{3}}(C_{11} - C_{12})d. \quad (5.1b)$$

In the VFF model,  $C_{44}$  can be calculated from  $\alpha$  and  $\beta$  as [36]

$$C_{44}^{VFF} = \frac{\sqrt{3}\alpha\beta}{(\alpha + \beta)d}. \quad (5.2)$$

Table 2: VFF parameters used for InAs and GaAs.  $\alpha$  and  $\beta$  calculated using Eqs. (5.1a) and (5.1b) with parameters from Table 1.  $d$  is from [54]. In-As-Ga parameters were obtained by averaging [55].

	$\alpha/\text{Nm}$	$\beta/\text{Nm}$	$d/\text{\AA}$	$\theta$
InAs	33.18	5.75	2.6220	109.5°
GaAs	39.58	9.18	2.4467	109.5°

In our calculations, we use the parameters from Table 1 for the bulk matrix and dot material. At the interface between the matrix and the dot material, a  $\beta$ -value is required for the In-As-Ga combination. This is done here by averaging. The parameter  $d$  is from [54]. Table 2 summarizes the values used in our calculations.

## 6 Boundary conditions

Quantum dots are often surrounded by a matrix material which is significantly larger than the dot itself so that it can be assumed to have an infinite extent. However, when solving the governing equations numerically, it is necessary to define a finite computational domain. Due to this, boundary conditions for the computational domain must be defined in such a way that the electromechanical field in the vicinity of the dot does not depend on this artificial boundary. To check whether the boundary conditions have a significant impact on the fields close to the dot the electromechanical fields in the vicinity of the dot are compared for different sizes of the computational domain. The strain fields are said to be converged with respect to domain size when changes in the strain fields close to the dot are negligible as the domain size is doubled. The different boundary conditions are compared and the best choice in terms of the smallest computational domain which ensures convergence of the strain fields is found.

### 6.1 Continuum model-strain fields

In this section, four different boundary conditions for the continuum model for a truncated pyramidal quantum dot with wetting layer are considered, see Fig. 1. The height from the top of the wetting layer to the top of the dot is 1.70nm, the wetting layer is 0.85nm thick, the side length at the top of the pyramid is 2.54nm, and the side length at the bottom of the pyramid is 5.93nm.

There are in principle infinitely many boundary conditions that could be considered at the artificial boundary and we will show that the precise choice of boundary conditions is not important for the electromechanical fields near the quantum dot. In this work, we choose primarily to consider the most common boundary conditions: Fixed, free, and periodic boundary conditions. The only exception is a mixed boundary conditions expected to be especially effective for quantum dot wetting layer structures.

### 6.1.1 Fixed boundaries

The simplest boundary condition to impose is the Dirichlet condition where the displacement vector is zero at the boundary, i.e.,

$$\mathbf{u}|_{\partial\Omega} = 0, \quad (6.1)$$

where  $\partial\Omega$  is the boundary of the computational domain  $\Omega$ .

In Fig. 7 we show the  $\varepsilon_{xx}$  component of the strain along the centerline  $(x,y) = (0,0)$  for four different domain sizes. Here, we see that there is a notable difference in the strain component going from the smallest domain to one twice as large. Only minor differences are obtained for larger domains as compared to the latter. This indicates that a domain size of 11nm is too small but a 22nm domain size ensures a negligible influence of the boundary condition on the strain in the vicinity of the dot.

The Dirichlet condition keeps the outer boundaries fixed, i.e., the quantum dot cannot easily expand (or contract) in this case. As we are interested in modeling a single quantum dot wetting layer structure in an infinite domain, a better condition might be to allow the outer boundaries to expand, i.e., implementing free boundary conditions.

### 6.1.2 Free boundaries

Free boundary conditions correspond to a vanishing net force on the boundary. Due to this the surface traction vector is required to be zero. The surface traction vector is given by

$$[T_n]_i = \sum_{j=1}^3 \sigma_{ij} n_j, \quad (6.2)$$

where  $\mathbf{n}$  is the outward pointing unit normal vector to the surface. The free boundary condition is then given by

$$\mathbf{T}_n|_{\partial\Omega} = \mathbf{0}. \quad (6.3)$$

In Fig. 8, we show the  $\varepsilon_{xx}$  component of the strain along the centerline  $(x,y) = (0,0)$  for four different domain sizes. Apparently, in order to ascertain a negligible influence of the boundary condition on the strain close to the dot we need a domain size of at least 45nm. This is twice as large compared to the fixed boundary case.

### 6.1.3 Periodic boundary conditions

Not much literature exists on the use of periodic boundary conditions in strain calculations. Imposing periodic boundary conditions is not a trivial task as the displacement vector is *not* required to be periodic because the structure is allowed to expand in all directions even for an array of quantum dots. We choose to define a set of periodic boundary conditions on one cell of the periodic structure (called the domain in the following) based on the following two principles.

The first principle is Newton's Second Law stating that, in the static case, the sum of all forces is zero. For a periodic array this entails that the traction force from one side of

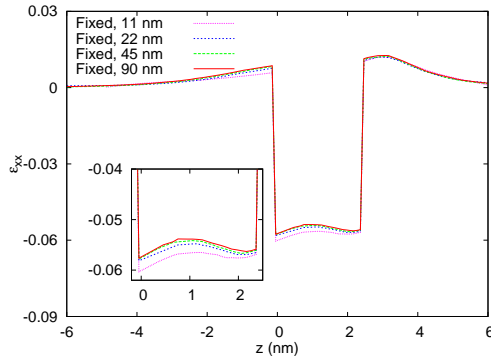


Figure 7: The  $\varepsilon_{xx}$  component of the strain along the centerline  $(x,y)=(0,0)$  for the four domain sizes 11nm, 22nm, 45nm, and 90nm. The strain field is found using fixed boundary conditions.

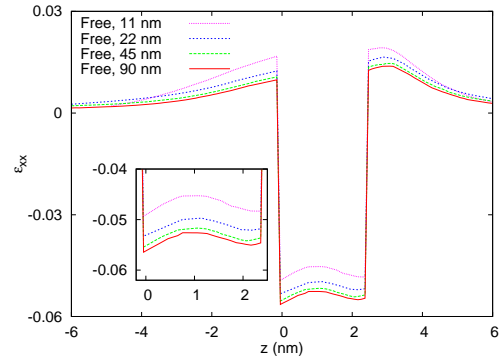


Figure 8: The  $\varepsilon_{xx}$  component of the strain along the centerline  $(x,y)=(0,0)$  for the four domain sizes 11nm, 22nm, 45nm, and 90nm. The strain field is found using free boundary conditions.

the domain plus the traction force from the other side of the domain must be equal to zero, i.e.,

$$\mathbf{T}_n|_{\partial\Omega_1} = -\mathbf{T}_n|_{\partial\Omega_2}, \tag{6.4}$$

where  $\partial\Omega_1$  and  $\partial\Omega_2$  are periodic boundaries.

The second principle states that no cracks are allowed to appear at the surface of the domain. This is satisfied if

$$\frac{\partial \mathbf{n} \cdot \mathbf{u}}{\partial \xi_i} \Big|_{\partial\Omega_1} = -\frac{\partial \mathbf{n} \cdot \mathbf{u}}{\partial \xi_i} \Big|_{\partial\Omega_2}, \tag{6.5}$$

where  $(\xi_1, \xi_2)$  are coordinates parameterizing the surface,  $\xi_3$  parameterizes the normal direction to the surface, and  $i=1,2,3$ . The minus sign takes into account that both normal vectors point out of the domain. The condition for  $i=1,2$  ensures that the slope of the two surfaces are equal while the last condition imposes the normal derivative of the displacement vector to be continuous at periodic boundaries. These boundary conditions were checked in the two-dimensional case in the paper by Lassen et al. [56].

In this paper, we use a rectangular box as domain with surfaces perpendicular to the  $x_1$ ,  $x_2$ , and  $x_3$  directions. The box is centered at  $(0,0,0)$ , so the outside surfaces are given

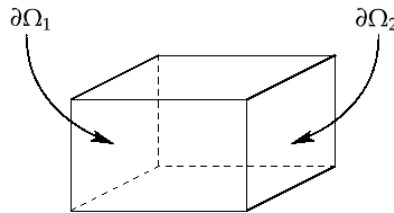


Figure 9: Schematic picture showing the computational domain together with two periodic boundaries  $\partial\Omega_1$  and  $\partial\Omega_2$ .

by

$$\partial\Omega_{1,\pm} = \left\{ (x_1, x_2, x_3) \mid x_1 = \pm \frac{L_1}{2} \right\}, \quad (6.6a)$$

$$\partial\Omega_{2,\pm} = \left\{ (x_1, x_2, x_3) \mid x_2 = \pm \frac{L_2}{2} \right\}, \quad (6.6b)$$

$$\partial\Omega_{3,\pm} = \left\{ (x_1, x_2, x_3) \mid x_3 = \pm \frac{L_3}{2} \right\}, \quad (6.6c)$$

where  $L_i$  is the length of the box in the  $x_i$  direction. In this case the periodic boundary conditions become

$$\sigma_{ji}|_{\partial\Omega_{i,+}} = \sigma_{ji}|_{\partial\Omega_{i,-}}, \quad \text{for } j=1,2,3, \quad (6.7a)$$

and

$$\frac{\partial u_i}{\partial x_j}|_{\partial\Omega_{i,+}} = \frac{\partial u_i}{\partial x_j}|_{\partial\Omega_{i,-}}, \quad \text{for } j=1,2,3, \quad (6.7b)$$

for  $i=1,2,3$ .

Unfortunately it turns out that the solution to the static strain equations is not unique when using these boundary conditions. This can easily be shown by considering the simple case of a quantum well, i.e., disregarding the truncated pyramid. It is known that the strain in an infinite quantum well is

$$\varepsilon_{xx} = \varepsilon_{yy} = \begin{cases} 0, & \text{outside the well,} \\ a, & \text{inside the well,} \end{cases} \quad (6.8a)$$

$$\varepsilon_{zz} = \begin{cases} 0, & \text{outside the well,} \\ -2a \frac{C_{12,q}}{C_{11,q}}, & \text{inside the well,} \end{cases} \quad (6.8b)$$

where  $C_{11,q}$  and  $C_{12,q}$  are the elastic modules of the quantum well material. This solution also satisfies the periodic boundary conditions mentioned above. Now consider the case:

$$\varepsilon_{xx} = \varepsilon_{yy} = \varepsilon_{zz} = \begin{cases} b, & \text{outside the well,} \\ a+b, & \text{inside the well,} \end{cases} \quad (6.9)$$

and

$$b = a \left( \frac{C_{11,b} + 2C_{12,b}}{C_{11,q} + 2C_{12,q}} - 1 \right)^{-1}, \quad (6.10)$$

where  $C_{11,b}$  and  $C_{12,b}$  are the elastic modules of the barrier material. This case can also be shown to be a solution to the problem with periodic boundary conditions. That is, we have at least two solutions to the problem when the truncated pyramid is disregarded. It is not difficult, however, to realize that the last solution is not physically relevant as the strain in this case exceeds  $-25\%$  thus violating the model assumption of linear elasticity.

When including the truncated pyramid, the second non-physical solution is unfortunately still a solution of the problem and there is no easy way of ensuring that a numerical scheme does not find this solution. Indeed, it turns out that when using the finite element method Comsol it is exactly the (physically) wrong solution that is found! Although it is interesting to come up with a solution to this problem this issue will not be pursued further in the present paper. Another reason behind this choice is that fixed boundary conditions work well!

#### 6.1.4 Mixed fixed free boundary conditions

It is widely accepted that for a quantum well the approximate infinite extent of the matrix material, assuming pseudomorphic growth, dictates the in-plane strain of the quantum well. However, in the quantum well growth direction the material is allowed to expand. This is still expected to be the case for the truncated pyramid with a wetting layer. A more appropriate set of boundary conditions is therefore to set the displacement in the direction perpendicular to the wetting layer growth direction to zero at the boundaries while keeping the rest of the boundary conditions free.

In Fig. 10, we show the  $\varepsilon_{xx}$  component of the strain along the centerline  $(x,y) = (0,0)$  for four different domain sizes. Comparing these results with the results for fixed boundary conditions (see Fig. 7) we see that the domain size can be chosen even smaller using fixed free boundary conditions.

#### 6.1.5 Comparison of the different boundary conditions

Finally, in Fig. 11 we show the  $\varepsilon_{xx}$  component of the strain along the centerline  $(x,y) = (0,0)$  obtained using the different boundary conditions given above. As expected, we see that as long as the computational domain is chosen large enough the strain in the vicinity of the dot does not depend on the specific boundary conditions chosen. Comparing the Figs. 7, 8, and 10 we observe that free boundary conditions require a computational box size of 45nm, fixed conditions a box size of 22nm, and fixed-free conditions a box size of 11nm. Based on this the best choice of boundary conditions for a quantum well wetting layer structure is to use the fixed-free boundary conditions. That this is a good choice is also apparent from Fig. 12, where we show the computational time for all calculations performed as a function of the number of degrees of freedom.

Our results confirm that electromechanical fields near the quantum dot are insensitive to the precise choice of boundary conditions at the artificial boundary. While this is not, in principle, a requirement, it is indeed fortunate as it allows us to choose the numerically most efficient form of the boundary conditions.

## 6.2 Continuum model-electric field

In this work we only consider the grounded boundary condition for the electric potential. This is done because it turns out that with this boundary condition the electric field is well

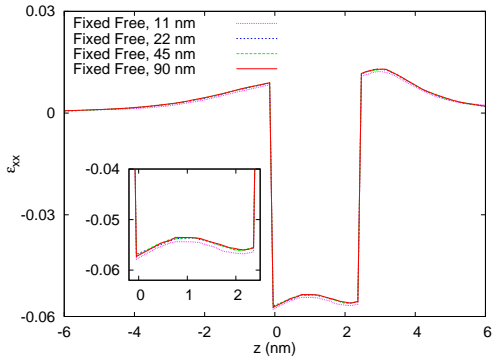


Figure 10: The  $\epsilon_{xx}$  component of the strain along the centerline  $(x,y)=(0,0)$  for the four domain sizes 11nm, 22nm, 45nm, and 90nm. The strain field is found using fixed free boundary conditions.

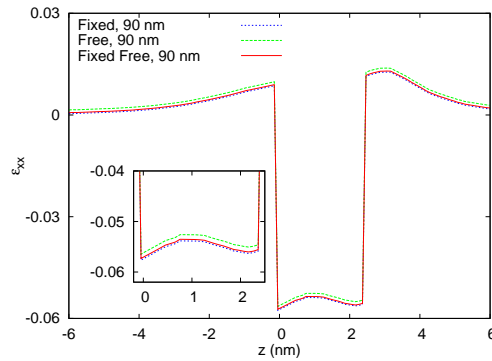


Figure 11: The  $\epsilon_{xx}$  component of the strain along the centerline  $(x,y)=(0,0)$  found using the Free, Fixed and Fixed Free boundary conditions.

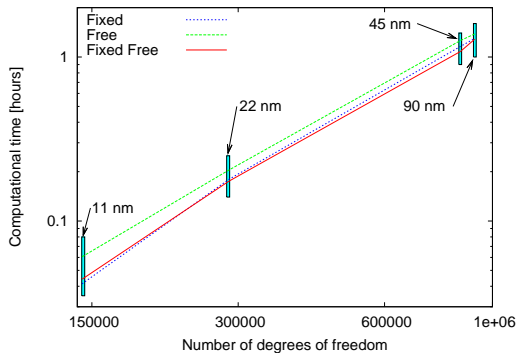


Figure 12: The computational time as a function of the number of degrees of freedom for Free, Fixed and Fixed Free boundary conditions. The boxes with associate text highlights the computational times associated with specific sizes of the computational domain.

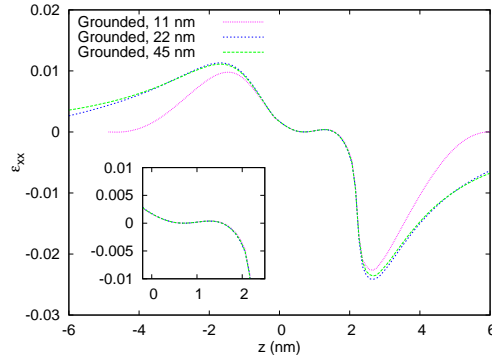


Figure 13: The electric potential  $V$  along the diagonal  $(z,z,z)$  as a function of  $z$  for the three domain sizes 11nm, 22nm, and 45nm.

captured in the vicinity of the dot for the computational domain size needed in order to capture the strain fields accurately.

The grounded boundary condition for the electric potential states that the electric potential at the boundary is constant. In this work we chose this constant to be zero, i.e.,

$$V|_{\partial\omega} = 0. \tag{6.11}$$

We show in Fig. 13 the electric potential along the diagonal line  $(z,z,z)$  as a function of  $z$  for three domain sizes. Here we see that the electric potential is indeed well captured within the dot region even for the smallest dot.

### 6.3 VFF

The Keating energy Eq. (4.4) contains a sum over all atoms as well as nearest neighbors. Interior atoms in InAs have four bonds to neighboring atoms while the number of bonds for atoms at the boundary of the computational domain depends on the choice of boundary conditions. We choose to consider the following four types of boundary conditions:

1. **Dangling bonds:** Bonds are cut off at the boundary and the atoms on the boundary have from zero to four bonds, depending on their position on the boundary (atoms with zero bonds can be removed entirely from the system).
2. **Periodic:** A computational box is defined and we demand that all atoms have four bonds. Bonds going out of the computational box will then enter again on the opposite side of the box. The box size itself is also subject to minimization by defining a spatially constant metric tensor, express the atom coordinates in terms of the metric, and optimize also with respect to the metric tensor components [57].
3. **Fixed:** As dangling bonds but with the atoms at the boundary held fixed at the corresponding positions in the reference configuration.
4. **Fixed Periodic:** As periodic but without optimization of the size of the computational box.

In Fig. 14 we show the effect of changing the computational box size for the four types of boundary conditions applied to the truncated pyramid quantum dot. In all cases, a square box with side lengths 11nm, 22nm, 45nm, and 90nm are considered. From Fig. 14 we see that the  $\epsilon_{xx}$  component of the strain along the center line  $(x,y)=(0,0)$  for small box sizes clearly deviates from the larger in the case of dangling bonds, periodic, and fixed boundary conditions. For fixed periodic boundary conditions, even the smallest box is almost indistinguishable from the largest. This highly favors the use of fixed periodic boundary conditions for calculations on isolated dots, since a computational box of 1/8th size compared to the 90nm box (needed for dangling bonds) corresponds to 1/512 the number of atoms, resulting in huge saving in memory and computational time for large dot sizes. Another good choice would be fixed boundary conditions, which are almost as good and easier to implement.

We must stress that for computations on isolated dots one should always perform a convergence analysis, similar to the one presented here, in order to determine the required box size.

Fig. 15 shows the computational time used to optimize the truncated pyramid for different number of atoms (computational domain sizes). The computational time is, however, in general affected not only by the total number of atoms, but also by the dot size, type of boundary conditions used, material parameters etc.

In Fig. 16 we further compare the dangling bonds and periodic boundary conditions. Close to the dot, we clearly see that the case with periodic boundary conditions match the case with dangling bonds closely but using a computational box of only half size.

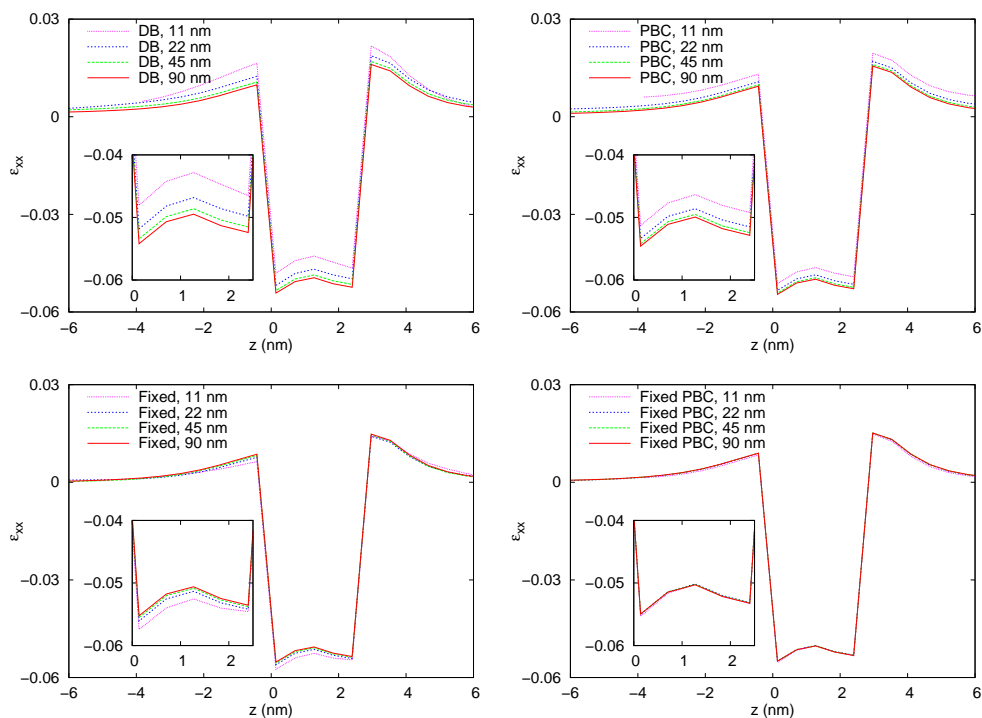


Figure 14:  $\epsilon_{xx}$  component, from VFF calculations, along the center line  $(x,y) = (0,0)$  of the truncated pyramid dot using dangling bonds (DB, Top Left), periodic (PBC, top right), fixed (Fixed, bottom left), and fixed periodic (Fixed PBC, bottom right) boundary conditions with computational box sizes with side length of 11nm, 22nm, 45nm, and 90nm. All results for fixed periodic boundary conditions are located, essentially, on top of one another.

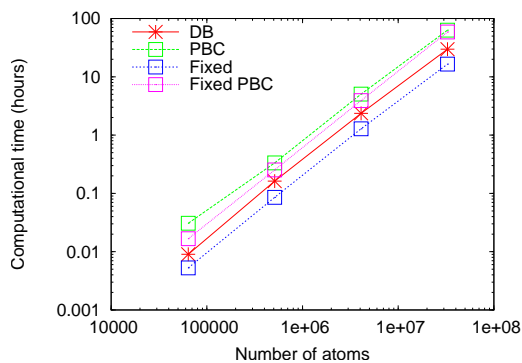


Figure 15: Computational time of the VFF calculations as a function of the total number of atoms for the truncated pyramid with dangling bonds (DB), periodic boundary conditions (PBC), fixed boundary conditions (Fixed), and fixed periodic boundary conditions (Fixed PBC). The computational domain is square with side lengths 11nm ( $\sim 6 \cdot 10^3$  atoms), 22nm ( $\sim 5 \cdot 10^5$  atoms), 45nm ( $\sim 4 \cdot 10^6$  atoms), and 90nm ( $\sim 3 \cdot 10^7$  atoms).

Far from the dot and near the boundary, the two cases show very different behaviours as expected.

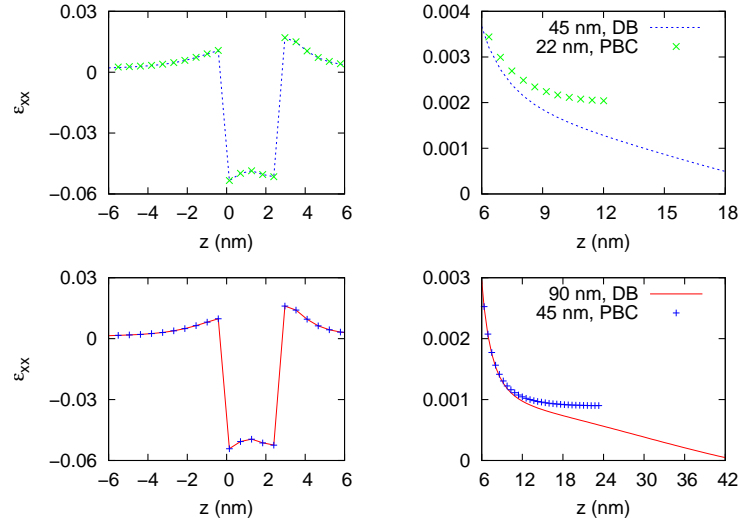


Figure 16:  $\varepsilon_{xx}$  component, from VFF calculations, along the center line  $(x,y) = (0,0)$  using periodic boundary conditions (PBC) and dangling bonds (DB) compared for different computational box sizes with the truncated pyramid dot. Periodic boundary conditions give essentially the same strain near the dot as dangling bonds, but using a computational box of half size.

## 7 Continuum vs VFF

In this section, we compare strain values found using the VFF approach with results of continuum calculations. We first consider spherical InAs quantum dots embedded in a GaAs matrix with radius  $R$  ranging from 1 to 4 nm. This is followed by a comparison for a cubic InAs quantum dot with side lengths  $l$  ranging from 1 to 8 nm again surrounded by a GaAs matrix. We finally show results for an InAs/GaAs truncated pyramidal quantum dot with wetting layer.

In the first (second) row of Fig. 17 we show the  $\varepsilon_{xx}$  ( $\varepsilon_{zz}$ ) strain component along the  $z$  axis for a spherical quantum dot with  $r = 1$  nm (left),  $r = 2$  nm (center), and  $r = 4$  nm (right) found using the following three different models: the VFF model, the continuum model with the correct  $C_{44}$  value, and the continuum model using  $C_{44}^{VFF}$  given by Eq. (5.2). We notice that both the continuum model with the correct and incorrect value of  $C_{44}$  give very similar results and that the VFF results deviate from the corresponding continuum results. This deviation is more evident for smaller quantum-dot structures, while it is of minor importance for the larger quantum dots.

In the first and second row of Fig. 18 we show the hydrostatic strain component:

$$\varepsilon_H(\mathbf{r}) = \varepsilon_{xx}(\mathbf{r}) + \varepsilon_{yy}(\mathbf{r}) + \varepsilon_{zz}(\mathbf{r}), \quad (7.1)$$

and the biaxial strain component:

$$\varepsilon_B(\mathbf{r}) = \varepsilon_{xx}(\mathbf{r}) + \varepsilon_{yy}(\mathbf{r}) - 2\varepsilon_{zz}(\mathbf{r}), \quad (7.2)$$

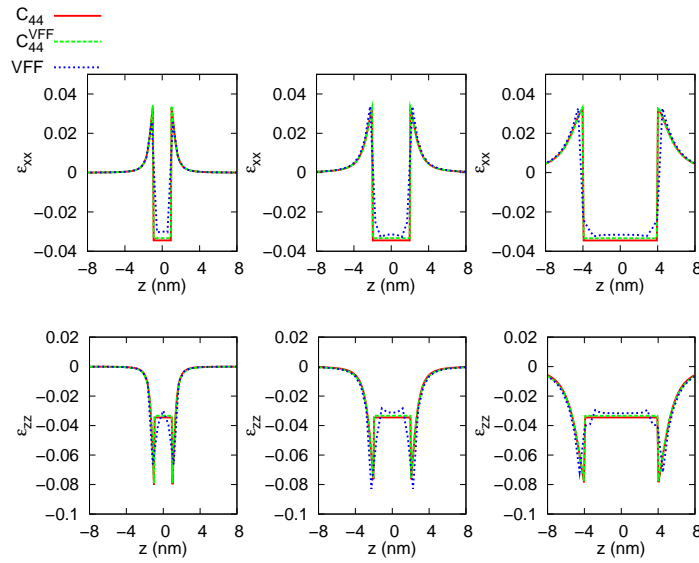


Figure 17: The  $\varepsilon_{xx}$  (top) and  $\varepsilon_{zz}$  (bottom) strain components along the  $z$  direction in the middle of the dot found using the continuum and the VFF models, for a spherical dot with radius  $r=1\text{nm}$  (left),  $r=2\text{nm}$  (center), and  $r=4\text{nm}$  (right).

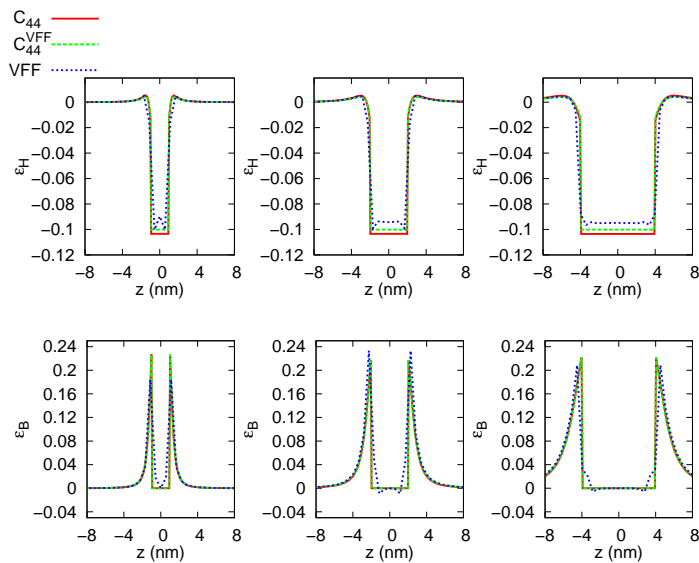


Figure 18: The  $\varepsilon_H$  (top) and  $\varepsilon_B$  (bottom) strain components along the  $z$  direction in the middle of the dot found using continuum and VFF models, for a spherical dot with radius  $r=1\text{nm}$  (left),  $r=2\text{nm}$  (center), and  $r=4\text{nm}$  (right).

along the  $z$  axis for spherical dots with the same radii and using the same models as for Fig. 17. Comparing the hydrostatic and biaxial components found based on the three models we see that they show the same tendencies as for the diagonal strain components.

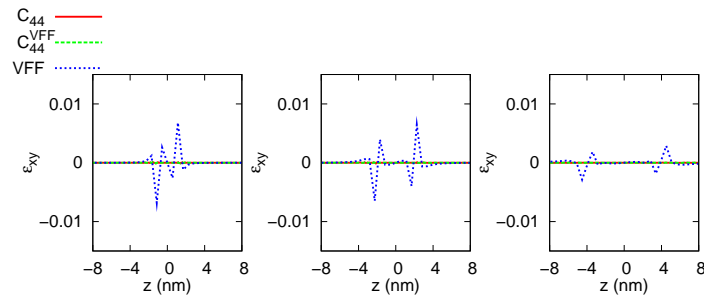


Figure 19: The  $\varepsilon_{xy}$  strain components along the  $z$  direction in the middle of the dot found using the continuum and VFF models, for a spherical dot with radius  $r=1\text{nm}$  (left),  $r=2\text{nm}$  (center), and  $r=4\text{nm}$  (right).

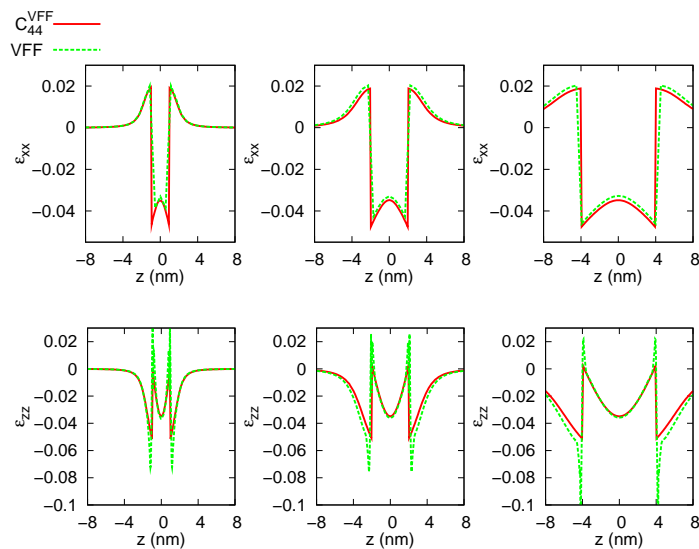


Figure 20: The  $\varepsilon_{xx}$  (top) and  $\varepsilon_{zz}$  (bottom) strain components along the  $z$  direction in the middle of the dot found using the continuum and VFF models, for a cube with side length  $l=2\text{nm}$  (left),  $l=4\text{nm}$  (center), and  $l=8\text{nm}$  (right).

This is expected as the hydrostatic and biaxial strain components are linear combinations of the diagonal strain components. We plot the hydrostatic and biaxial strain components as they directly influence the electronic structure of quantum dots as discussed in the next section.

Fig. 19 shows the off-diagonal strain component  $\varepsilon_{xy}$  found using both the continuum models and the VFF model. Within the continuum framework the off-diagonal strain components are zero, while the atomistic VFF results show a non-negligible component which decreases as the radius of the dot is increased. This deviation can be explained by the fact that for the smaller dots the real zincblende crystal structure does not give rise to the perfect spherical shape used in the continuum models. However, as the size of the dot increases, the atomistic structure more closely resembles a perfect sphere. This obviously

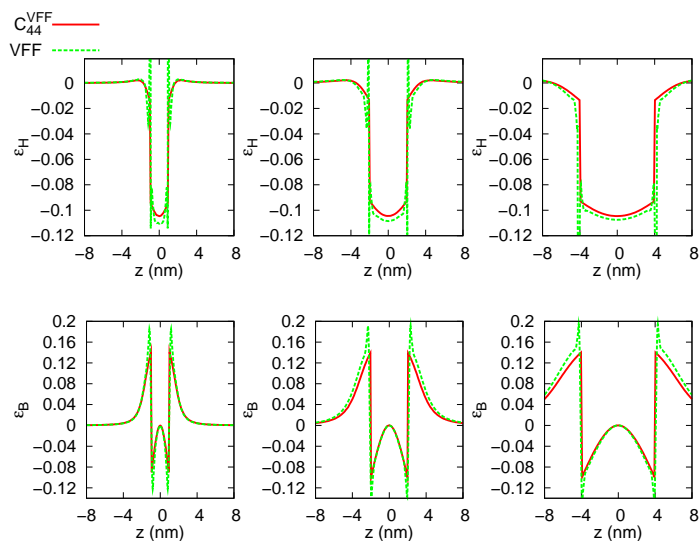


Figure 21: The  $\varepsilon_H$  (top) and  $\varepsilon_B$  (bottom) strain components along the  $z$  direction in the middle of the dot according continuum and VFF model, for a cube with  $l=2\text{nm}$  (left),  $l=4\text{nm}$  (center), and  $l=8\text{nm}$  (right).

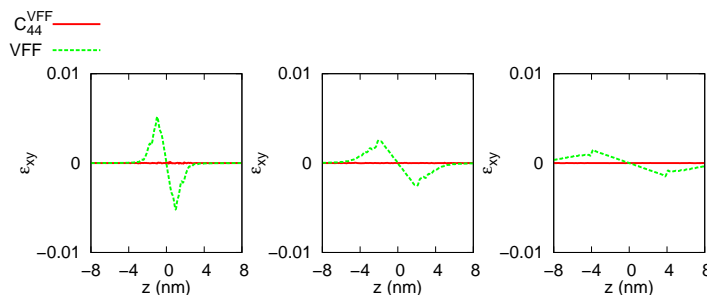


Figure 22: The  $\varepsilon_{xy}$  strain components along the  $z$  direction in the middle of the dot according continuum and VFF model, for a cube with  $l=2\text{nm}$  (left),  $l=4\text{nm}$  (center), and  $l=8\text{nm}$  (right).

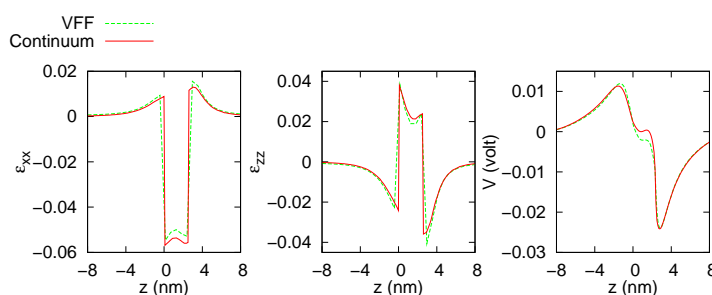


Figure 23: The  $\varepsilon_{xx}$  (left) and the  $\varepsilon_{zz}$  (center) strain components along the  $z$  direction through the middle of the dot found using the continuum and VFF models, for a truncated pyramidal dot with height from the top of the wetting layer to the top of the dot of  $1.70\text{nm}$ , wetting layer thickness of  $0.85\text{nm}$ , length at the top of the pyramid of  $2.54\text{nm}$ , and length at the bottom of the pyramid of  $5.93\text{nm}$ . The right figure shows the electric potential along the  $(z, z, z)$  line as a function of  $z$ .

indicates some limitations of continuum vs. atomistic models for smaller quantum-dots. The observed differences are expected to be relevant for electronic bandstructure and optical properties. In fact, in the eight-band model  $k \cdot p$  there is a direct contribution from the off-diagonal strain components [34].

To confirm our conclusions concerning differences between the results given by the continuum model and the VFF model, we study three cubic structures with side lengths  $l = 2\text{nm}$ ,  $l = 4\text{nm}$ , and  $l = 8\text{nm}$ , respectively. As for the spherical dots we plot, in Fig. 20, the  $\varepsilon_{xx}$  and  $\varepsilon_{zz}$  strain components along the  $z$  direction in the first and second row, respectively, and in Fig. 21 we show the  $\varepsilon_H$  and  $\varepsilon_B$  components along the  $z$  direction. Here we consider only results given by the VFF model and the continuum model with  $C_{44}^{VFF}$ . From these figures, it is clear that a very good quantitative and qualitative agreement between the two models is found-also for the smallest structure. In the case of a cubic shape the zincblende crystal structure is coincident with the shape of the heterostructure, supporting our claim that the deviations observed for the spherical shape indeed are due to the crystal structure not coinciding with the shape of the heterostructure studied in the continuum framework.

This is also confirmed by the results plotted in Fig. 22. Here we show the  $\varepsilon_{xy}$  strain component along the  $z$  direction in the middle of the dot found using the continuum and the VFF model. Although there is an off-diagonal component different from zero in the VFF model, the value for the smallest dot is four times smaller than in the corresponding case of a spherical dot modelled using continuum theory.

Finally, we compare the strain fields found using the VFF and the continuum approaches for the truncated pyramid. In Fig. 23 we show the  $\varepsilon_{xx}$  and  $\varepsilon_{zz}$  strain components along the center of the dot in the  $z$  direction. Again we see the same trends as for the spherical and cubic quantum dots revealing that the previous conclusions also hold for more realistic quantum dot shapes. In Fig. 23, (right) the electric potential is shown along the diagonal (i.e., along the  $(z, z, z)$  line) using both the VFF and the continuum approach. From this figure we see that there is a notable deviation between the two models inside the dot where the continuum approach gives a vanishing electric potential while the VFF approach gives rise to a non zero potential. However, the deviation, being small, is not expected to have a large impact on electronic properties.

## 8 Inhomogeneous concentration profiles

In this section, we study in the framework of the continuum model spherical  $\text{In}_c\text{Ga}_{1-c}\text{As}$  quantum dots with radii  $R = 1, 2, 4\text{nm}$  embedded in a GaAs matrix. Two cases are compared corresponding to a homogeneous concentration and a linear concentration profile ( $c = 1 - r/R$ ) where  $r$  is the distance from the center of the sphere. Investigations are carried out for an average In content decreasing in steps of 15% from 100% to 55%.

In Fig. 24, we show contour plots for a spherical quantum dot with radius 1nm and  $c = 1$  (left column) and a linear  $c$  profile (right column). In the first row, the  $\varepsilon_{xx}$  profile

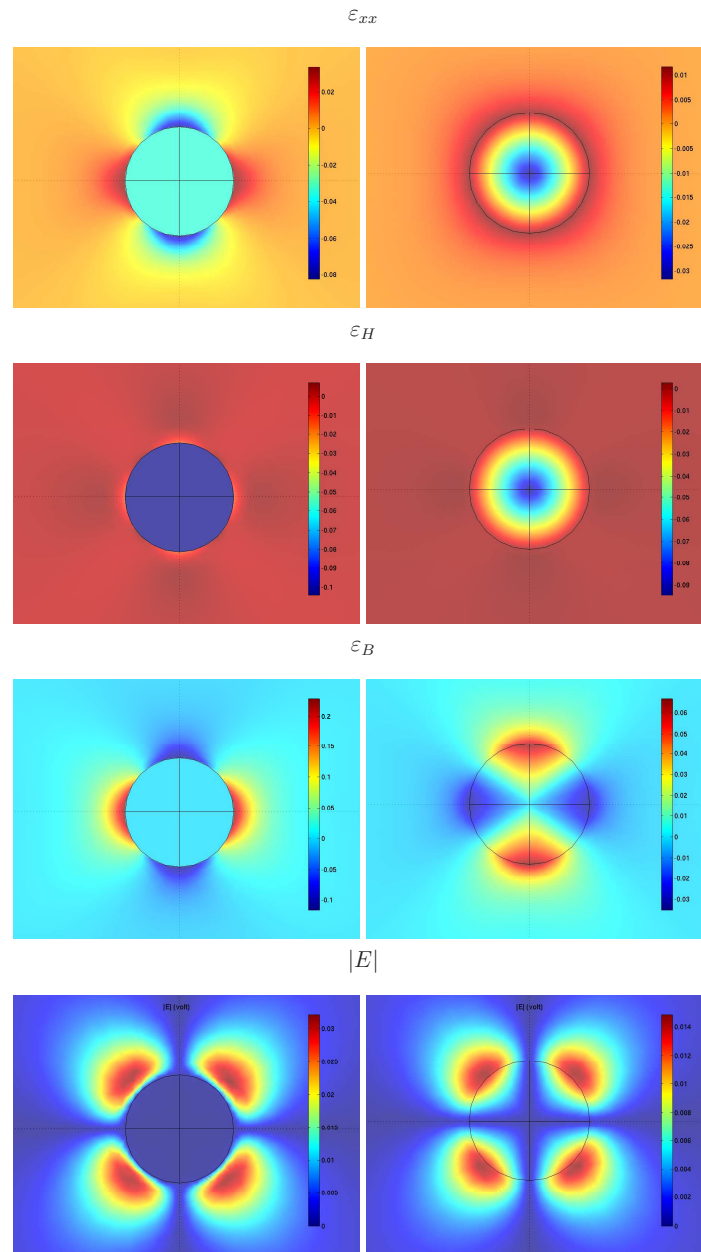


Figure 24: The  $\varepsilon_{xx}$  strain component (first row), the hydrostatic component  $\varepsilon_H$  (second row), the biaxial component  $\varepsilon_B$  (third row), and the absolute value of the electric field (last row) for a quantum dot with  $c=1$  and linear  $c$  in the first and second column, respectively.

in the  $xz$  plane is shown while the hydrostatic potential  $\varepsilon_H(\mathbf{r})$  is depicted in the second row. As expected, the plots reveal that the linear strain profile induces a considerable more inhomogeneous strain profile inside the quantum dot. However, even when  $c=1$ , a

slight anisotropy is observed. This is due to the anisotropic zincblende crystal structure. This anisotropy entails the necessity of developing a complete three-dimensional model, since an analytical isotropic solution for a spherical dot, similar to the one given in [37], does not include the full symmetry of the problem.

In the third row, the biaxial strain component  $\varepsilon_B(\mathbf{r})$  is given. In the homogeneous case, the biaxial strain is zero inside the dot but for a linear concentration profile the biaxial strain is nonzero and depends on the radial coordinate. It decreases linearly through the dot being zero only at the center of the sphere. Furthermore, the absolute value of the electric field, which is plotted in the last row in the  $xy$  plane, shows a similar behavior. While the biaxial strain is nonzero only outside the dot in all cases with a homogeneous concentration, the biaxial strain also penetrates into the dot in the case of a linear concentration profile. These features, when concentration gradients are present, are expected to significantly influence the electronic states inside the dot [38–40].

In the first and second rows of Fig. 25 we plot the  $\varepsilon_{xx}$  and  $\varepsilon_{zz}$  strain components along the  $z$  direction through the middle of the dot for all  $c$  values with radii 1nm (left), 2nm (center), and 4nm (right). As expected, we observe in cases with a homogeneous concentration that the strain increases as a function of the concentration  $c$ . This is predominantly due to an increase in the lattice mismatch between the dot and the matrix material. In the case of a linear concentration profile, we find a linear decrease of the strain components inside of the dot as the radial coordinate approaches the dot radius.

In the first and second rows of Fig. 26 we plot the hydrostatic  $\varepsilon_H$  and biaxial  $\varepsilon_B$  strain components along the  $z$  axis (i.e., through the middle of the dot) with  $R = 1\text{nm}$  (left),  $R = 2\text{nm}$  (center), and  $R = 4\text{nm}$  (right). These strain components are important since they appear directly in the effective potential for electronic states. If we consider, for simplicity, a one-band model, the strain dependent part of the electron Hamiltonian for a zincblende crystal structure is given by [27]

$$H_v^\varepsilon(\mathbf{r}) = a_c(\mathbf{r})\varepsilon_H(\mathbf{r}), \quad (8.1)$$

where  $a_c$  is the conduction-band hydrostatic deformation potential [58]. In the case of a homogeneous concentration, we only obtain an energetic shift for the bound electronic states and hence no effect on the *location* of electronic states while, in the case of a linear concentration profile, the electron wave functions are located closer to the edge of the sphere, due to  $a_c$  being negative for both InAs and GaAs [36].

The situation is more complicated for the hole states. In this case, the strain dependent part is given by

$$H_h^\varepsilon(\mathbf{r}) = a_v(\mathbf{r})\varepsilon_H(\mathbf{r}) \pm \frac{b(\mathbf{r})}{2}\varepsilon_B(\mathbf{r}), \quad (8.2)$$

where  $a_v$  and  $b$  are the valence-band hydrostatic deformation potential and the shear deformation potential, respectively [58], and the  $+$  ( $-$ ) sign is used for heavy (light) holes. It should be noted that the literature values of  $a_v$  are indecisive as they vary in the range:

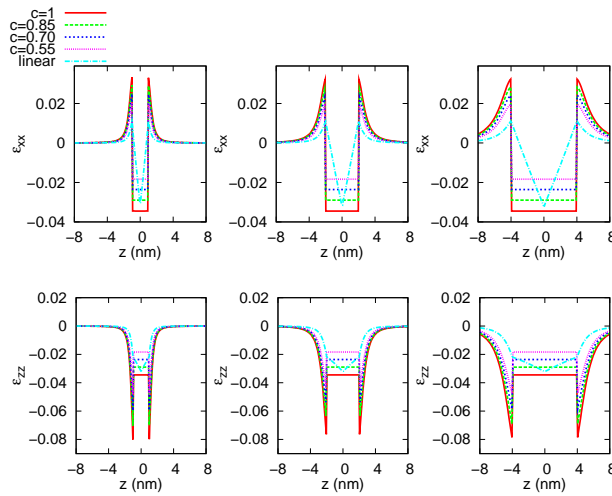


Figure 25: The  $\epsilon_{xx}$  (top) and  $\epsilon_{zz}$  (bottom) strain components along the  $z$  direction through the middle of the dot for different  $c$  values. The dot radii are: 1nm (left), 2nm (center), and 4nm (right).

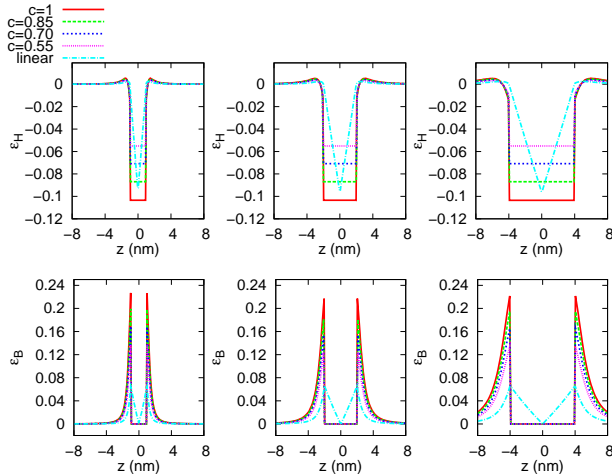


Figure 26: The hydrostatic  $\epsilon_H$  (top) and biaxial  $\epsilon_B$  (bottom) strain components along the  $z$  direction through the middle of the dot for different  $c$  values. The dot radii are 1nm (left), 2nm (center), and 4nm (right).

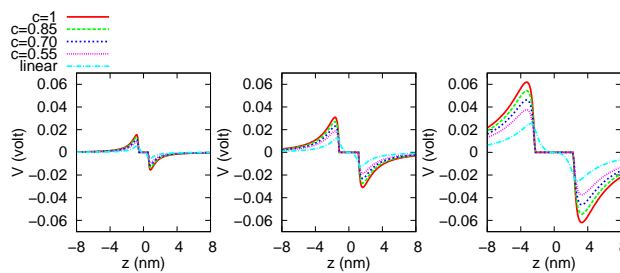


Figure 27: The electric potential along the  $x=y=z$  direction as a function of  $c$  for a dot with  $R=1$ nm (left),  $R=2$ nm (center), and  $R=4$ nm (right).

$-1\text{eV}$  to  $1\text{eV}$  [35], so it is not known whether the impact of the hydrostatic strain component leads to an increase or a decrease of the confinement potential! The behavior of the biaxial strain component is noteworthy. This component is zero inside a pure InAs quantum dot as well as a homogeneous  $\text{In}_c\text{Ga}_{1-c}$ . As quantum dot, hence it does not contribute to the effective potential inside the dot. But in the case of a linear concentration profile,  $\varepsilon_B$  is positive inside the dot and characterized by a linear decrease towards the dot radius. Since  $b$  is negative, the heavy hole state is located closer to the edge while the light hole is confined near the center of the dot. The latter effects strongly affect the overlap of the electron and hole wave functions and ultimately the optical strength of the interband transitions. In [36], a reduction of the overlap has been observed for the groundstate transition where it was attributed to induced symmetry breaking as a result of the piezoelectric effect. However, it was recently shown that the effect of an inhomogeneous biaxial strain field may also lead to a decreasing or an increasing overlap between the conduction and valence band wave functions [59].

Finally we plot in Fig. 27 the electric potential along the diagonal:  $x=y=z$ . Again we find for a homogeneous concentration that the potential is zero inside the dot while, in the case of a linear concentration profile,  $V$  is zero only at the center of the sphere. These differences significantly affect the location and overlap of electron and hole wavefunctions.

## 9 Conclusions

In this work the following three main topics were studied. First, an investigation into optimal boundary conditions on the computational domain for single quantum dots was performed. Second, a detailed comparison between the atomistic valence force method (VFF) and continuous strain theory was carried out. And finally, the effect of changing the In concentration profiles in InAs/GaAs quantum dots was investigated.

For the atomistic VFF method it was shown that by choosing fixed periodic boundary conditions the size of the computational domain could be reduced by 1/8th compared with the case of using dangling bonds. For continuous strain theory it turned out that by imposing periodic boundary conditions the solution to the governing equations was not unique anymore making it difficult to find the physical relevant solution. In addition to periodic boundary conditions both free and fixed boundaries were studied. It was shown that the best choice in this case is to use fixed boundary conditions. Additionally, it was shown that for quantum dots with a wetting layer, a better choice is to use a mixed boundary condition.

The comparison between the atomistic VFF method and continuous strain theory showed an excellent agreement between the two for dot sizes larger than 2nm. It was shown that the main source of deviations between the two models for smaller dots was the incompatibility of the chosen shape of the quantum dot in the continuous model with the zincblende crystal structure present in the VFF model.

Within the framework of continuous strain theory it was shown that changing the concentration profile of the quantum dot has a significant impact on the strain fields as well as the electric field inside the quantum dot. This difference will have a direct impact on optical and electronic properties of the quantum dots showing that it is necessary to include more realistic concentration profiles in the study of optoelectronic properties of quantum dots.

## References

- [1] P. Y. Yu and M. Cardona, *Fundamentals of Semiconductors-Physics and Materials Properties*, Third Ed., Springer Berlin, 2005.
- [2] T. Ando, A. Fowler and F. Stern, Electronic properties of two-dimensional systems, *Rev. Mod. Phys.*, 54 (1992), 437.
- [3] I. N. Stranski and L. Krastanow, *Sitzungsberichte der Akademie der Wissenschaften in Wien, Abteilung IIb*, 146 (1937), 797.
- [4] V. Ya Prinz, D. Grutzmacher, A. Beyer, C. David and B. Ketterer, A new technique for fabricating three-dimensional micro- and nanostructures of various shapes, *Nanotechnology*, 12 (2001), 399–402.
- [5] O. G. Schmidt and K. Eberl, Nanotechnology: thin solid films roll up into nanotubes, *Nature*, 410 (2001), 168.
- [6] S. Tanda, T. Tsuneta, Y. Okajima, K. Inagaki, K. Yamaya and N. Hatakenaka, Crystal topology: a Mbius strip of single crystals, *Nature*, 417 (2002), 397.
- [7] Z. Hens, D. Vanmaekelbergh, E. J. A. J. Stoffels and H. van Kempen, Effects of crystal shape on the energy levels of zero-dimensional PbS quantum dots, *Phys. Rev. Lett.*, 88 (2002), 236803.
- [8] X. Duan, C. Niu, V. Sahi, J. Chen, J. W. Parce, S. Empedocles and J. L. Goldman, High-performance thin-film transistors using semiconductor nanowires and nanoribbons, *Nature*, 425 (2003), 274.
- [9] P. X. Gao, Y. Ding, W. Mai, W. L. Hughes, C. Lao and Z. L. Wang, Conversion of zinc oxide nanobelts into superlattice-structured nanohelices, *Science*, 309 (2005), 1700.
- [10] M. H. Huang, S. Mao, H. Feick, H. Yan, Y. Wu, H. Kind, E. Weber, R. Russo and P. Yang, Room-temperature ultraviolet nanowire nanolasers, *Science*, 292 (2001), 1897.
- [11] S. Lal, S. Link and N. J. Halas, Nano-optics from sensing to waveguiding, *Nature Photonics*, 1 (2007), 641–648.
- [12] L. Guy, S. Muensit and E. M. Goldys, Electrostriction in gallium nitride, *Appl. Phys. Lett.*, 75 (1999), 3641–3643.
- [13] R. E. Newnham, V. Sundar, R. Yimnirun, J. Su and Q. M. Zhang, Electrostriction: nonlinear electromechanical coupling in solid dielectrics, *J. Phys. Chem. B*, 101 (1997), 10141.
- [14] M. Willatzen and L. C. Lew Yan Voon, Static and dynamic effects due to electrostriction in GaN/AlN, *J. Phys. Cond. Matter*, 19 (2007), 506202.
- [15] I. Kornev, M. Willatzen, B. Lassen and L. C. Lew Yan Voon, Electrostriction coefficients of GaN, AlN, MgO and ZnO in the wurtzite structure from first-principles, *AIP Conf. Proc.*, 1199 (2010), 71.
- [16] M. Willatzen, B. Lassen and L. C. Lew Yan Voon, Nonlinearities and piezoelectric fields in AlN/GaN wurtzite heterostructures, *J. Appl. Phys.*, 100 (2006), 124309.

- [17] L. C. Lew Yan Voon and M. Willatzen, Electromechanical phenomena in semiconductor nanostructures, *J. Appl. Phys.*, 109 (2011), 031101.
- [18] T. Saito and Y. Arakawa, Electronic structure of piezoelectric In<sub>0.2</sub>Ga<sub>0.8</sub>N quantum dots in GaN calculated using a tight-binding method, *Phys. E*, 15 (2002), 169.
- [19] B. Lassen, M. Willatzen, D. Baretin, R. V. N. Melnik and L. C. Lew Yan Voon, Electromechanical effects in electron structure for GaN/AlN quantum dots, *J. Phys. Conf. Series*, 107 (2008), 012008.
- [20] E. Pan, Elastic and piezoelectric fields in substrates GaAs (001) and GaAs (111) due to a buried quantum dot, *J. Appl. Phys.*, 91 (2002), 6379.
- [21] H. J. Chu, E. Pan, J. J. Ramsey, J. Wang and C. X. Xue, A general perturbation method for inhomogeneities in anisotropic and piezoelectric solids with applications to quantum-dot nanostructures, *Int. J. Solids Struct.*, 48 (2011), 673–679.
- [22] M. J. P. Musgrave and J. A. Pople, A general valence force field for diamond, *Proc. Roy. Soc. London Ser. A*, 268 (1962), 474.
- [23] M. A. Nusimovici and J. L. Birman, Lattice dynamics of wurtzite: CdS, *Phys. Rev.*, 156 (1967), 925.
- [24] P. N. Keating, Effect of invariance requirements on the elastic strain energy of crystals with application to the diamond structure, *Phys. Rev.*, 145 (1966), 637–645.
- [25] R. M. Martin, Dielectric screening model for lattice vibrations of diamond-structure crystals, *Phys. Rev.*, 186 (1969), 871–884.
- [26] R. M. Martin, Elastic properties of ZnS structure semiconductors, *Phys. Rev. B*, 1 (1970), 4005–4011.
- [27] V. A. Fonoberov and A. A. Balandin, Excitonic properties of strained wurzite and zincblende GaN/Al<sub>x</sub>Ga<sub>1-x</sub>N quantum dots, *J. Appl. Phys.*, 94 (2003), 7178–7186.
- [28] John H. Davies, Elastic and piezoelectric fields around a buried quantum dot: a simple picture, *J. Appl. Phys.*, 84 (1998), 1358.
- [29] I. P. Ipatova, V. G. Malyshkin and V. A. Shchukin, On spinodal decomposition in elastically anisotropic epitaxial films of III-V semiconductor alloys, *J. Appl. Phys.*, 74 (1993), 7198.
- [30] B. Jogai, J. D. Albrecht and E. Pan, Effect of electromechanical coupling on the strain in AlGaN/GaN heterojunction field effect transistors, *J. Appl. Phys.*, 94 (2003), 3984.
- [31] M. Willatzen, B. Lassen, L. C. Lew Yan Voon and R. V. N. Melnik, Dynamic coupling of piezoelectric effects, spontaneous polarization, and strain in lattice-mismatched semiconductor quantum-well heterostructures, *J. Appl. Phys.*, 100 (2006), 024302.
- [32] B. Lassen, R. V. N. Melnik and M. Willatzen, Spurious solutions in the multiband effective mass theory applied to low dimensional nanostructures, *Commun. Comput. Phys.*, 6 (2009), 699–729.
- [33] P. W. Fry, I. E. Itskevich, D. J. Mowbray, M. S. Scolnick, J. J. Finley, J. A. Barker, E. P. O'Reilly, L. R. Wilson, I. A. Larkin, P. A. Maksym, M. Hopkinson, M. Al-Khafaji, J. P. R. Davis, A. G. Cullis, G. Hill and J. C. Clark, Inverted electron-hole alignment in InAs-GaAs self-assembled quantum dots, *Phys. Rev. Lett.*, 84 (2000), 733–736.
- [34] Y. Zhang, Motion of electrons in semiconductors under inhomogeneous strain with application to laterally confined quantum wells, *Phys. Rev. B*, 49 (1994), 14352–14366.
- [35] A. Schliwa, M. Winkelkemper and D. Bimberg, Impact of size, shape, and composition on piezoelectric effects and electronic properties of In(Ga)AsGaAs quantum dots, *Phys. Rev. B*, 76 (2007), 205324.
- [36] O. Stier, M. Grundmann and D. Bimberg, Electronic and optical properties of strained quantum dots modeled by 8-band  $k \cdot p$  theory, *Phys. Rev. B*, 59 (1999), 5688–5701.

- [37] D. Bimberg, M. Grundmann and N. N. Ledentsov, *Quantum Dot Heterostructures*, John Wiley & Sons, 1999.
- [38] C. Pryor, M-E. Pistol and L. Samuelson, Electronic structure of strained InP/Ga<sub>0.51</sub>In<sub>0.49</sub>P quantum dots, *Phys. Rev. B*, 56 (1997), 10404.
- [39] A. D. Andreev and E. P. O'Reilly, Theory of the electronic structure of GaN/AlN hexagonal quantum dots, *Phys. Rev. B*, 62 (2000), 15851.
- [40] B. Jogai, Free electron distribution in AlGa<sub>N</sub>/Ga<sub>N</sub> heterojunction field-effect transistors, *J. Appl. Phys.*, 91 (2002), 3721–3729.
- [41] J. Piprek, *Nitride Semiconductor Devices-Principles and Simulation*, Wiley-VCH, 2007.
- [42] J. A. Barker and E. P. O'Reilly, Theoretical analysis of electron-hole alignment in InAs-GaAs quantum dots, *Phys. Rev. B*, 61 (2000), 13840–13850.
- [43] C. Cornet, A. Schliwa, J. Even, F. Dor, C. Celebi, A. Ltoublon, E. Mac, C. Paranthou, A. Simon, P. M. Koenraad, N. Bertru, D. Bimberg and S. Loualiche, Electronic and optical properties of InAs/InP quantum dots on InP(100) and InP(311)B substrates: theory and experiment, *Phys. Rev. B*, 74 (2006), 035312.
- [44] T. Inoue, O. Wada, M. Konno, T. Yaguchi and T. Kamino, Electron tomography of embedded semiconductor quantum dots, *Appl. Phys. Lett.*, 92 (2008), 031902.
- [45] L. D. Landau and E. M. Lifshitz, *Theory of Elasticity*, Course of Theoretical Physics, Vol. 7, Pergamon Press, 1970.
- [46] S. L. Chuang, *Physics of Photonic Devices*, Wiley, 2009.
- [47] K. Biswas, A. Franceschetti and S. Lany, Generalized valence-force-field model of (Ga,In)(N,P) ternary alloys, *Phys. Rev. B*, 78 (2008), 085212.
- [48] S. Madsen and F. Jensen, Locating seam minima for macromolecular systems, *Theor. Chem. Acc.*, 123(5-6) (2008), 477.
- [49] J. Nocedal and S. J. Wright, *Numerical Optimization*, Springer-Verlag New York, 1999.
- [50] R. Renka, Algorithm 660: QSHEP2D: Quadratic shepard method for bivariate interpolation of scattered data, *ACM Trans. Math. Software*, 14 (1988), 149–150.
- [51] P. M. Gullett, M. F. Horstemeyer, M. I. Baskes and H. Fang, A deformation gradient tensor and strain tensors for atomistic simulations, *Model. Simul. Mater. Sci. Eng.*, 16 (2008), 015001.
- [52] E. Pan, Elastic and piezoelectric fields around a quantum dot: fully coupled or semicoupled model?, *J. Appl. Phys.*, 91 (2002), 3785–3796.
- [53] L. Duggen and M. Willatzen, Crystal-orientation effects on wurtzite quantum-well electromechanical fields, *Phys. Rev. B*, in Press, 2010.
- [54] S. Chen, X. G. Gong and S. H. Wei, Ground-state structure of coherent lattice-mismatched zinc-blende A<sub>1-x</sub>B<sub>x</sub>C semiconductor alloys ( $x=0.25$  and  $0.75$ ), *Phys. Rev. B*, 77 (2008), 073305.
- [55] J. Z. Liu, G. Triamrchi and A. Zunger, Strain-minimizing tetrahedral networks of semiconductor alloy, *Phys. Rev. Lett.*, 99 (2007), 145501.
- [56] B. Lassen, P. Wang, R. Jones and X. Zhang, Fully coupled electromechanical model for dielectric elastomer sheets, *IEEE Trans. Mech.*, in Press, 2010.
- [57] M. Parrinello and A. Rahman, Crystal structure and pair potentials: a molecular-dynamics study, *Phys. Rev. Lett.*, 45 (1980), 1196–1199.
- [58] G. L. Bir and G. E. Pikus, *Symmetry and Strain-Induced Effects in Semiconductors*, Wiley New York, 1974.
- [59] D. Baretin, J. Houmark, B. Lassen, M. Willatzen, T. R. Nielsen, J. Mørk and A.-P. Jauho, Optical properties and optimization of electromagnetically induced transparency in strained InAs/GaAs quantum dot structures, *Phys. Rev. B*, 80 (2009), 235304.